Chemical Engineering Journal 425 (2021) 130606

Contents lists available at ScienceDirect

Chemical Engineering Journal

journal homepage: www.elsevier.com/locate/cej

The electrosorption characteristics of simple aqueous ions on loofah-derived activated carbon decorated with manganese dioxide polymorphs: The effect of pseudocapacitance and beyond

Yu-Jen Shih [a,*], Yun-Ru Chen [a], Ching-Lung Chen [b,c], Jui-Yen Lin [d], Chin-Pao Huang [e]

[a] Institute of Environmental Engineering, National Sun Yat-sen University, Kaohsiung, Taiwan
[b] Department of Safety, Health and Environmental Engineering, Ming Chi University of Technology, New Taipei City, Taiwan
[c] Center for Environmental Sustainability and Human Health, Ming Chi University of Technology, New Taipei City, Taiwan
[d] Institute of Analytical and Environmental Sciences, National Tsing Hua University, Hsinchu 300, Taiwan
[e] Department of Civil and Environmental Engineering, University of Delaware, Newark, DE 19716, USA

ARTICLE INFO

Keywords:
Electrosorption
Pseudocapacitance
Differential capacitance
modified Langmuir adsorption isotherm
Isoelectric point

ABSTRACT

The capability of manganese dioxide (MnO_2) supported on loofah-derived activated carbon (AC) in the electrosorptive removal of common inert ions was studied in constant potential mode. Four MnO_2 polymorphs were prepared by redox chemical precipitation and characterized by XRD, SEM, BET and XPS. The pseudocapacitance property of the MnO_2/AC electrode, significantly affected by the surface- and diffusion-controlled charge storage mechanism, was assessed via voltammetry and modified Langmuir adsorption isotherm. Batch electrosorption experiments were then performed at constant potential in the range of −1.5 V to + 1.5 V (vs. Ag/AgCl) using AC and α-MnO_2/AC electrodes in the presence of common simple electrolytes, including $NaNO_3$, Li_2SO_4, and Ca$(ClO_4)_2$. Consequently, the applied working potential (E_{app}) positively affected the ion electrosorption rate and capacity. Faradaic processes occurred on MnO_2, i.e., Mn(III)/Mn(IV) transition, increased the diffusion capacitance of AC, thus enhancing the first-order rate and monolayer capacity, mainly for the electrosorption of cations. Results showed that ion solvation, controlled by the ionic radius and valence of an ion, which impacted ion intercalation in MnO_2 and affected ion adsorption characteristics. The cation sorption capacity of α-MnO_2/AC followed the order of Na^+ (2.8×10^{-4} mol g^{-1}) > Ca^{2+} (2.1×10^{-4} mol g^{-1}) > Li^+ (0.76×10^{-4} mol g^{-1}) at E_{app} = -1.5 V. The differential capacitance as affected by polarized potential and the shift of zero net charge or IEP toward more positively charging potential further highlighted the contribution of pseudocapacitance to ion adsorption on α-MnO_2/AC electrode.

1. Introduction

There is a severe worldwide water scarcity, mostly in the Middle East, continental Africa, and Southern Asia [1]. Desalination, specifically, the removal of salts and unwanted ions from sea or brackish water sources, has been commonly thought after as a means to extract fresh water. Water reclamation and reuse programs have been implemented in many regions of the world as to meet high water demands for public drinking, agricultural, and industrial uses [2]. Currently, commercially available technologies such as thermal distillation (multi-stage flash and multiple effect distillation) and membrane separation (reverse osmosis) are able to supplement global water demands by desalination to a great extent [3]. However, high energy consumption in thermal treatment and high capital and operational costs in membrane technology are primary drawbacks, which has prompted the development of new desalination technologies. Adsorption is a low-cost technique for the separation and removal of salts and other ionic or molecular contaminants from waters [4]. Adsorption has been examined for salt removal using carbon-based materials, such as activated carbon, carbon nanotubes, graphene, of which could be derived from natural, agricultural and industrial waste biomass [5]. However chemical regeneration of spent adsorbents is inevitable for reusing adsorbents, which can involve the further use of regenerating chemicals such as concentrated strong acids or bases or chelation agents.

Capacitive deionization (CDI) has been considered a potential alternative to current water purification practices such as desalination

* Corresponding author.
E-mail address: yjshih@mail.nsysu.edu.tw (Y.-J. Shih).

https://doi.org/10.1016/j.cej.2021.130606
Received 16 February 2021; Received in revised form 25 May 2021; Accepted 27 May 2021
Available online 2 June 2021
1385-8947/© 2021 Elsevier B.V. All rights reserved.

[6], softening [7], and metal recovery [8], in the last decades. Carbon materials, such as activated carbon and graphene are commonly used CDI electrodes due to high specific surface area, porous structures, cost effective, and electrochemically stable features [9]. Cations and anions can be electrostatically trapped in the symmetrically porous and high surface area electrodes, during cathodic and anodic charging, respectively. Reverse charging readily releases the adsorbed ions and regenerates the electrodes accordingly. Further, in energy field, some redox promoters, normally transition-metal oxides, such as TiO_2, SnO_2, MnO_2, $CoFe_2O_4$, have been employed as supercapacitors [10-13]. The characteristics of metal oxide capacitance, i.e., pseudocapcitance, is originated from the lattice spacing amenable to ion storage during faradaic electron transfer in different metal states [14] (Eq. (1)):

$$Me^{IV}O_2 + \delta(1-nf)H^+ + \delta e^- + \delta f M^{n+} \rightarrow H_{(1-nf)\delta}M^{n+}_{f\delta}Me^{III}_{\delta}Me^{IV}_{1-\delta}O_2 \quad (1)$$

$Me^{IV}O_2$ and M^{n+} denote the pseudocapacitive metal oxide and metal ion, respectively. Among transition-metal oxides, MnO_2 is particularly attractive because of its low cost and high theoretical specific capacitance [15]. MnO_2 has multiple crystallographic phases, namely, α-, β-, γ-, δ-, λ-, and ε-MnO_2, which are characterized by the linkage of MnO_6 octahedron unit. The efficiency of cations (M^{n+}) transporting within the MnO_2 polymorph depends on the effective ion radius and the size of charged Mn-O lattice spacing [16]. Ion adsorption capacity of electrodes having intercalation with MnO_2 composites was typically greater than that of porous carbon materials alone [17].

The effectiveness of electrode materials in deionization has been investigated in numeral CDI studies, including the conductivity of the solution, the voltage and current profiles, charge efficiency, and energy consumption [18]. NaCl is normally the model salt to study the adsorption capacity and rate of CDI systems [19]. A general CDI desalination was performed at applied voltage of 1.2 V during ion removal operation and at 0 or < 0 V for electrode regeneration [20-22]. The surface chemistry of ideal polarizable electrodes (IPE), i.e., non-faradaic charging materials, critically influences the ion storage. The specific and selective adsorption among potential determining ions (pdi) may affect the treatment efficiency of complex ion composition in wastewaters. Dried Loofah is a typical agricultural waste product and has been previously applied as the biomass precursor for the synthesis of activated carbon (AC). The porosity and disordering of carbon structure could be manipulated via heating treatment; the surface area of AC from the one-step activation (with $ZnCl_2$ at 500 °C) was up to 1500 m^2 g^{-1}. The loofah-derived AC has high carbon purity with<1 wt% of ash content and exhibited significant ammonium ion (NH_4^+) electrosorption capacity at a negative polarity (E_{app} = -1.0 V vs. Hg/HgO) [23]

At present, the electrical double-layer (EDL) and pseudocapacitive CDI systems are developed for desalination. There are several CDI designs, e.g., pseudocapacitive//EDL [24], pseudocapacitive//pseudocapacitive [25], EDL//EDL [26], battery-type//EDL [27], desalination batteries [28], and pseudocapacitive//battery-type deionization [29]. Among the above CDI systems, pseudocapacitive//EDL is the most common design for water purification applications due to its robust ion adsorption/desorption and storage functionalities. Although the principle of pseudocapacitor is highly attractive for enhancing the performance of CDI systems, little is known about the characteristics and mechanism of electrosorption of common cations and anions with respect to electrostatic interactions or intercalation of MnO_2. It is hypothesized that the crystal structure of pseudocapacitors will affect the ion separation capacity of carbon-based electrodes. In this work, a series of MnO_2 nanoparticulates with different crystal phases and morphology were synthesized and incorporated into a loofah-derived activated carbon electrode for studying the separation of selected simple ions. The working potential (from −1.5 V to + 1.5 V vs. Ag/AgCl) was applied to assess the ion adsorption characteristics of carbon and MnO_2/carbon composites. For an asymmetric sorption of ions, the electroneutrality may cause pH fluctuation, i.e., H^+/OH^- concentration changes, during electrosortpion process. Note that H^+ has the highest equivalent ionic conductivity, λ (349.8 S-cm^2/eq), among all ions, for instance, 50.11 and 76.34 S-cm^2/eq for Na^+ and Cl^-, respectively [30,31]. The measurements of conductivity alone may not be sufficient for determining CDI effectiveness when specific chemical adsorption of certain cations or anions take place on the electrode surface. Therefore, ion adsorption capacity was monitored by direct analytical determination and described by a modified Langmuir adsorption isotherm instead of conductivity measurements, an approach practiced by most CDI researchers. Since the intrinsic chemical properties of target ions determine their selectivity in separation and purification processes, specifically by electrostatic force, such as adsorption and electrosorption. In order to demonstrate the effects of the type and charge of ions on the electro-sorption capacity of MnO_2/carbon composites, inert ionic species such as Li^+, Na^+, Ca^{2+}, NO_3^-, ClO_4^-, and SO_4^{2-}, or simple salts i.e., $NaNO_3$, Li_2SO_4, and $Ca(ClO_4)_2$, were used as model electrolytes in this study.

2. Materials and methods

2.1. Electrode materials

The synthesis of activated carbon (AC), derived from an agricultural residue of dried ripened *Luffa cylindrica*, was reported previously [23,32]. The biochar precursor was carbonized at 500 °C under N_2 gas, followed by pyrolsys at 800 °C and activation by $ZnCl_2$ (Sigma-Aldrich Co., USA) to synthesize the AC.

Procedure for preparing different MnO_2 polymorphs was as the following: (1) A mixture of 0.01 M of $MnSO_4$ (Sigma-Aldrich Co.) and 0.01 M of $KMnO_4$ (Nippon Shinyaku, Japan) was stirred to allow self-redox reaction between Mn(II) and Mn(VII) and subsequent precipitation of α-MnO_2 under 95 °C [33]; (2) γ-MnO_2 was prepared from the precipitation of solution containing 0.1 M of $MnSO_4$ (Sigma-Aldrich Co.) and 0.1 M of $Na_2S_2O_8$ (PanReac AppliChem) as oxidizing agent [34]; (3) δ-MnO_2 was made by reducing 0.4 M of $KMnO_4$ with 1.4 M of glucose ($C_6H_{12}O_6$, PanReac AppliChem) at 85 °C followed by annealing at 450 °C for 2 h [28]; (4) ε-MnO_2 was prepared the oxidation of 0.01 M of $MnSO_4$ (Sigma-Aldrich Co.) by 0.1 M of NaOCl (12 wt%, Nippon Shinyaku) at pH 5.5 and 80 °C [35]. All chemical reactions were carried out in 200 mL of solution. All prepared MnO_2(s) samples were rinsed thoroughly in deionized (DI) water until the supernatant reached neutral pH. A specific weight of AC was simultaneously being soaked in above manganese solutions while redox reaction was taking place as to load MnO_2 precipitates on AC. In this work, around 5% of MnO_2 were loaded onto AC.

AC and MnO_2 were further ground in a pestle and mortar and then sieved through ASTM #100 mesh (<74 μm). The MnO_2/AC powders were used for surface characterization and electrode preparation. Graphite plate (2 mm thick), purchased from Great Carbon Co., Ltd., Taiwan, was used as the support for MnO_2/AC electrodes. The electrode paste composed of MnO_2/AC, poly(vinylidene fluoride) (PVDF) as binder (~5%), and N-Methyl-2-pyrrolidone (NMP) (Sigma-Aldrich Co.) as solvent was mixed and degassed in a centrifugal mixer (at 1200 rpm). The paste was evenly spread on the graphite surface with a paint brush, and then dried at 105 °C for 24 h.

2.2. Experimental procedure

A potentostat (CHI611C, CH Instruments, Inc., USA) was used to conduct electrochemical analyses in a three-electrode system with Ag/AgCl/NaCl (3 M) (RE-1B, ALS Co. Ltd., JAPAN), MnO_2/AC, and IrO_2/Ti as the reference, working, and counter electrodes, respectively. Batch electrosorption was performed in a polymethyl methacrylate (PMMA)-made electrochemical cell, consisting of two parallel plate electrodes. A spacer at a distance of 0.5 cm was sandwiched between the two electrodes (Fig. S1). The working electrode of MnO_2/AC/graphite was cut into a dimension of 5 × 5 cm^2 (total area ~ 25 cm^2) and the counter electrode was IrO_2/Ti mesh, having the same dimension as the MnO_2/AC/graphite. The polarity of working electrode was adjusted in the constant potential range of −1.5 V to + 1.5 V vs. Ag/AgCl during electrosorption experiments. The working solutions were prepared in synthetic water containing $NaNO_3$, Li_2SO_4, and $Ca(ClO_4)_2$ electrolytes. Water samples were taken at specific time intervals to analyze the concentration of corresponding cations and anions.

2.3. Surface analysis

A scanning electron microscope (SEM, JSM-6700F, JEOL, Tokyo, Japan), integrated with an energy dispersive spectroscopy (EDS, INCA400, Oxford, UK), and a transmission electron microscope (FEG-TEM, Tecnai F20 G2, USA) were used to observe the morphology of AC and MnO_2/AC electrodes. The crystallographic structure of MnO_2 polymorphs was observed using X-ray diffraction (XRD, Bruker D2-Phaser, Bruker, USA) under conditions of Cu Kα source (λ = 1.5406 Å), scan rate = 0.06° s^{-1}, incidence angle = 10-80° (2θ). The oxidation state of Mn was determined by X-ray photoelectron spectroscopy (XPS, PHI 5000 VersaProbe, Physical Electronics, Inc., USA) with a monochromatic Al Kα X-ray source (1487 eV). Specific surface area and porosity were examined by a BET analyzer (ASAP 2020, Micromeritics, USA). Ion concentrations were determined by ion chromatography (ECO IC, Metrohm, Switzerland) using separation columns of Metrosep A supp 5 and Metrosep C – 4 for anions and cations, respectively.

3. Results and discussion

3.1. Surface characterization

Fig. 1a-d show the SEM micromorphology of MnO_2 polymorphs, corresponding to α-, ε-, δ-, and γ-MnO_2, respectively. The α-MnO_2 appeared as one-dimensional (1-D) whisker-like crystallite with a particle size of few tens of nanometer in diameter and several μm in length (Fig. 1a). The material prepared by the reduction of Mn^{VII} has been proven to be α-phase [36] based on the three major facets (2 1 1), (3 1 0), and (2 0 0) at 2θ of 37.5°, 28.8°, and 18.1°, respectively (#44–0141) from X-ray diffractometer as shown in Fig. 2a. The main peaks at 2θ of 37.3°, 56.2°, and 66.0° could be attributed to the (1 0 0), (1 0 2), and (1 1 0) planes of hexagonal akhtenskite, ε-MnO_2 (#30–0820) [37], which were nanoplates, with 200 nm in diameter and 50 nm in thickness (Fig. 1b). δ-MnO_2 exhibited porous 3-D porous balls in the size range of 100–500 nm which were built by interleaving nano-flaks (Fig. 1c). The δ-MnO_2 was characterized by the two basal planes of (0 0 1) and (0 0 2) at 2θ of 12.5° and 25.2°, respectively, with layer spacing of around 7 Å (Birnessite, #80–1098) [38]. The randomly distributed nano-needles of γ-MnO_2 as shown in Fig. 1d had peaks of (1 2 0), (1 3 1), and (3 0 0) at 2θ of 22.4°, 37.1°, and 42.6°, respectively (#14–0644) [39]. The carbonized and activated loofah sponge (AC) had a fiber texture of ~ 100 μm in diameter (Fig. 1e), in which the tubular pore structure could be uniformly filled by MnO_2 nanoparticles to form the MnO_2/AC composite (Fig. 1f). TEM images revealed that the diameter of α-MnO_2 whiskers was in the range of 10 – 50 nm, well distributed over the carbon surfaces (Fig. 1g & h).

Fig. 2b presents the oxidation state of Mn in all MnO_2 samples via the XPS analysis. The two binding energies (B.E.) at around 642 eV and 654 eV were ascribed to the $2p_{3/2}$ and $2p_{1/2}$ band of Mn orbitals, respectively [40]. The B.E. in the $2p_{3/2}$ region was deconvoluted to oxidation states of Mn(III) (MnOOH, Mn_2O_3) and Mn(IV) (MnO_2) at 641.9 eV and 643.3 eV, respectively [41], and hence the atomic ratio of Mn(III/IV) was quantified. Result showed that the percentage of Mn(IV) followed the order of α-MnO_2 (70%) > γ-MnO_2 (59%) > δ-MnO_2 (57%) > ε-MnO_2 (52%). The presence of Mn(III) indicated the presence of oxygen vacancies in MnO_2 [42]. Two implications rose. First, the net surface charge, created from different oxidation state of Mn lattices (IV to III), was balanced by the intercalated cations (i.e., Na^+) during capacitive charging. Second, Mn(IV), high Mn oxidation state, was active electrochemical feature of MnO_2-based electrodes [43]. Both polymorph and defect could play critical roles in electrochemical energy storage, which in turn governed the ion sorption capacity. The specific surface area and porosity of MnO_2 and MnO_2/AC composite were characterized by BET measurements shown in Fig. 2c & 2d. The specific surface area of MnO_2 was generally low, around a few tens of an m^2 g^{-1}; among all polymorphs, δ-MnO_2 had the highest BET surface area of 193 m^2 g^{-1}, which could be ascribed to its 3-D morphology. By contrast, the carbon substrate (AC), derived from an agricultural biomass, i.e., dried loofah [23], exhibited a significantly high surface area of 752 m^2 g^{-1}. Furthermore, the hysteresis loop in the isotherm suggested capillary condensation in mesopores [22]. Whereas, the BET surface area of AC improved slightly after decoration with MnO_2 (5%) (801 m^2 g^{-1}).

3.2. Electrochemical features of MnO_2 polymorph

Typically, an electrical-double-layer capacitor (EDLC) has a cyclic voltammogram (CV) that is symmetrical and near rectangular in the specific range of scanning potential. As shown in Fig. 3a, the loofah-carbon electrode revealed a simple EDL capacitor character. A pseudo-capacitor, such as MnO_2, is characterized by distinct charge transfer peaks (resulted from specific faradaic redox reactions on the electrode surface) that increase with increasing electrolyte concentration (Fig. 3b, Fig. S2). The differential capacitance,C_E, defined as the change of charge density (σ, C g^{-1}) per change of specific surface potential (Ψ) over the electrode, could be obtained from voltammetry according to the

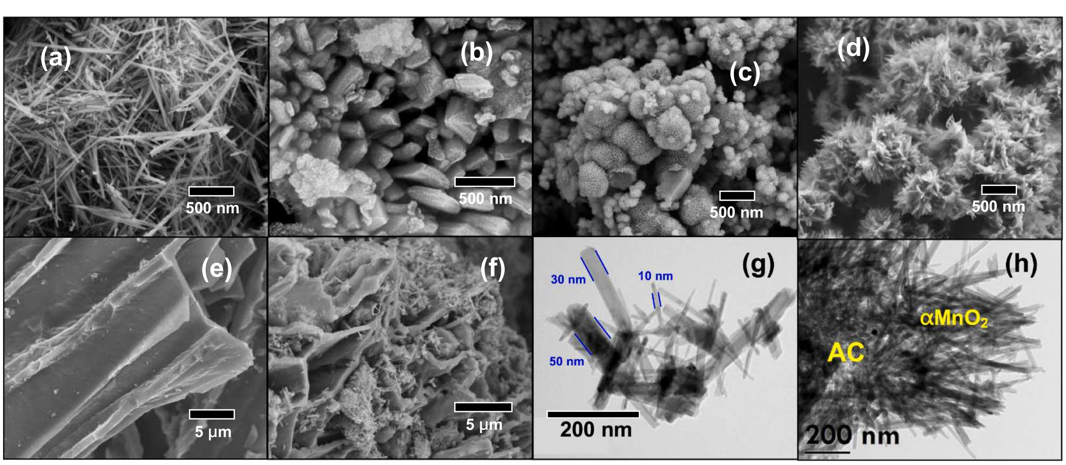

Fig. 1. SEM micromorphology of (a) α-, (b) ε-, (c) δ-, (d) γ-MnO_2, (e) AC, and (f) αMnO_2/AC; TEM analysis of (g) α-MnO_2 and (h) αMnO_2/AC.

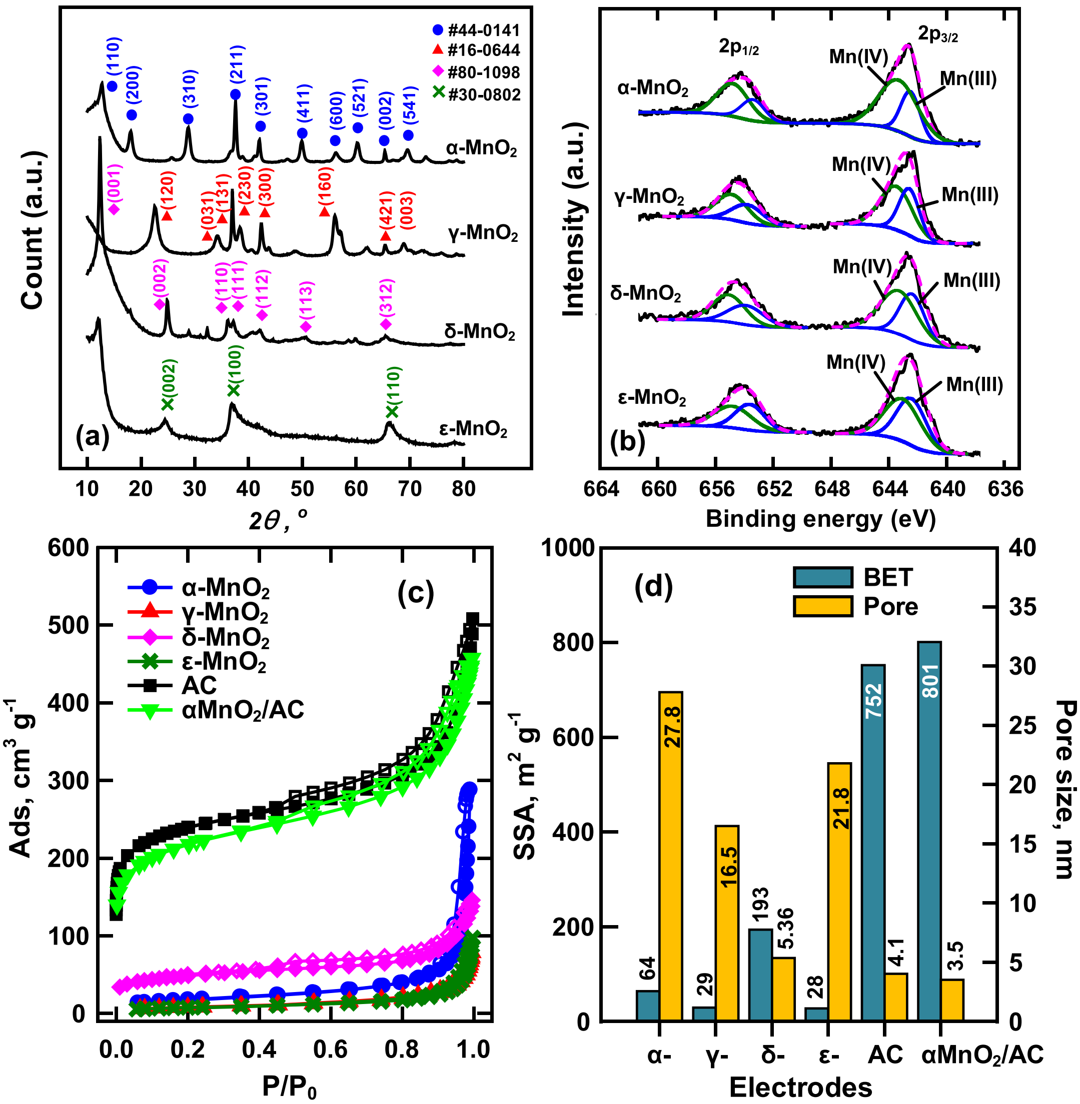

Fig. 2. (a) XRD, (b) XPS analyses, and (c) BET isotherms of AC and MnO_2 polymorphs. (d) Specific surface area and pore size of different electrodes.

following equation [44,45]:

$$C_E = \frac{d\sigma}{d\Psi} = \frac{\int_{V_1}^{V_2} (I_a - I_c)dE}{m \times v \times \Delta E}(F/g) \quad (2)$$

where E is the polarizable potential (V), v is the voltage scan rate ($V\ s^{-1}$), m is the active mass of the electrode (g), I_a and I_c are the anodic and the cathodic current, respectively (A), V_1 and V_2 are the integration boundary of the polarizable voltage (V), respectively. ΔE is the range of applied voltage, $= V_2 - V_1$. Note that charge is the product of current (I, A) and time (t, sec), which equals the energy density (I × E) divided by scan rate ($v = dE/dt$). Hence, Eq. (2) gives the total capacity of the differential capacitance of the electrode as charging ions in the selected range of working potential, ΔE [46,47].

Moreover, since the electrode potential (*E*) was swept reversely at a given rate ($v = dE/dt$), the surface-controlled (i.e., EDL) capacitance is linearly related to current, I, and scan rate, v [48]:

$$C_E = d\sigma/dE = Idt/dE = I/v \quad (3)$$

Eq. (3) gives the intensity of differential capacitance at specific polarizable potential, E.

For diffusion control redox reaction, i.e., typical pseudocapactors, the diffusional current is defined by the Randles-Sevcik equation as follows:

$$I = 0.4958nFAC * D^{1/2}(\alpha nF/RT)^{1/2} v^{1/2} \quad (4)$$

where n is number of electron; F is Faraday constant ($C\ mol^{-1}$); A is effective area (cm^2); C* is electrolyte concentration ($mol\ cm^{-3}$); D = diffusion coefficient of redox species ($cm^2\ s^{-1}$); α = transfer coefficient. That is, CV current of a typical pseudocapacitor is diffusion-controlled and is positively proportional to the square root of v. In the presence of pseudocapacitor, the total charging current density, $i(E, v)$, is the sum of that of EDL (non-Faradic) and diffusion [48,49]:

$$i(E, v) = a_1 v + a_2 v^{1/2} \quad (5)$$

Eq. (5) can be rearranged by dividing all terms by $v^{1/2}$, which yields the following equation:

$$\frac{i(E, v)}{v^{1/2}} = a_1 v^{1/2} + a_2 \quad (6)$$

A plot of $\frac{i(E,v)}{v^{1/2}}$ vs. $v^{1/2}$ gives intercept and slope for a_1 and a_2, respectively, at specific polarizing potential, E. The non-Faradaic current from the charging of surface-controlled EDL is calculated from a_1. The I_{diff} component can be calculated from the a_2 value at specific E. Accordingly, the component capacitance of non-Faradaic (EDL) and pseudocapacitive (diffusion) charging can be determined from Eq. (3).

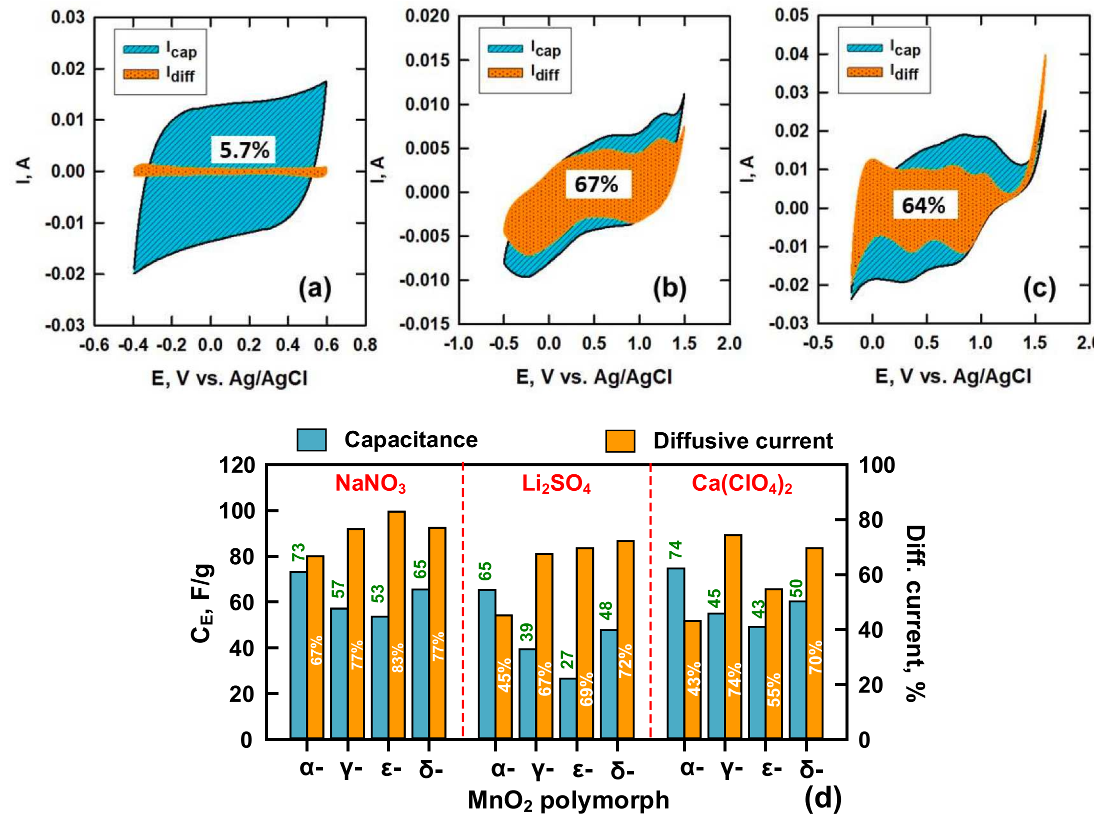

Fig. 3. Cyclic voltammetry of (a) AC, (b) α-MnO_2, and (c) αMnO_2/AC electrodes (0.1 M $NaNO_3$, scan rate = 10 mV s^{-1}). (d) Electrical capacitance of MnO_2 polymorphs in different electrolytes (I = 10^{-1} M) estimated by CV analysis.

For example, at a scan rate of 10 mV s^{-1}, 5.7% and 67% of the total charge were attributed to diffusive current (I_{diff}, area marked in orange color) for AC and α-MnO_2, respectively (Fig. 3a and b). Results indicated the contribution of redox reaction (pseudocapacitive) to activated carbon (AC) in the presence of α-MnO_2 was 64% (Fig. 3c) due to I_{diff} while charging the αMnO_2/AC composite electrode. The incorporation of MnO_2 (about 5%) onto AC (a pure EDL capacitor having surface-controlled current of 94.3%), readily converted MnO_2/AC electrode to a pseudocapacitor.

Fig. 3d summarizes the fraction of diffusive current and total capacitance of MnO_2 polymorphs in the presence of different electrolytes (ionic strength = 10^{-1} M). The C_E value typically followed the order: α-MnO_2 > γ-MnO_2 > δ-MnO_2 > ε-MnO_2. Moreover, the type of electrolyte also affected the total capacitance: $NaNO_3$ > $Ca(ClO_4)_2$ > Li_2SO_4. The contribution of redox process to C_E also differed; the diffusive current was on average high in the presence of $NaNO_3$, implying that the intercalation mechanism may be limited by the ion species. The diversity of MnO_x states (II, III or IV) provides net charges in crystal lattices during redox process and the resistance of ion transport is then determined by the lattice shapes [50,51]. Based on the stacking of MnO_6 octahedron (tunnel-shaped α-MnO_2 with [2 × 2] tunnels and γ-MnO_2 with [1 × 2] tunnels, layered δ-MnO_2 with [1×∞] planes, and hierarchically porous ε-MnO_2 with [1 × 1] or [1 × 2] tunnels, the interstitial space of α-MnO_2, γ-MnO_2, δ-MnO_2, and ε-MnO_2 were 6, 2.3, 1.89, and 1.89 Å, respectively [52,53]. Meanwhile, several factors of aqueous electrolytes, such as concentration, hydrated ion radius, conductivity, and ion mobility affected the electrochemical capacitance [54]. In the organic electrolyte system, Li^+ generally in forms of $LiPF_6$ and $LiClO_4$, was mostly used in batteries due to its smallest ionic size among the alkali metals, which enables easy lattice intercalation. However, ion solvation of cations alters the nature of ion transport in the aqueous electrolyte. A significant difference in the specific capacitance of graphene electrode was reported for different chloride salts: HCl > KCl > NaCl > LiCl [55]. Moreover, pseudocapacitor stores charge not only in form of EDL but also via reversible redox reactions. The fast insertion of ions on the electrode surface thereby achieved high fraction of diffusive capacitance.

3.3. Batch electrosorption of selective electrolytes

Fig. 4 demonstrates the electrosorption of $NaNO_3$ on αMnO_2/AC electrode at different initial $NaNO_3$ concentrations of 10 to 50 mg- L^{-1} based on NO_3^--N. The adsorption of Na^+ and NO_3^- were recorded at constant potentials of 0 to −1.5 V and 0 to + 1.5 V (vs. Ag/AgCl), respectively, for 90 min, followed by desorption of both Na^+ and NO_3^-, at 0 V for 20 min. The removal of Na^+ and NO_3^- increased with increasing applied counter voltage was due to strong electrostatic field. The decrease in removal efficiency of Na^+ and NO_3^- with increase in initial $NaNO_3$ concentration increases was ascribed to surface site saturation. The first-order kinetics rate law better describe the removal of electrolyte, both cationic and anionic, as the following:

$$-\frac{dC}{dt} = k_1(C - C_e) \tag{7a}$$

or

$$C_t = C_e + (C_0 - C_e)e^{-k_1 t} \tag{7b}$$

where C_0 and C_e stand for the initial and equilibrium ion concentrations (mg L^{-1}), respectively. (C_e was estimated by least-squares regression). In order to assess the removal rate of different electrolytes, a series of sorption/desorption experiments were run on AC and α-MnO_2/AC electrodes at −1.5 to + 1.5 V vs. Ag/AgCl. The rate constant, k_1, for the electrosorption of different electrolytes, namely, Li_2SO_4, $NaNO_3$, and $Ca(ClO_4)_2$, obtained from the corresponding experimental data (Fig. S3 to

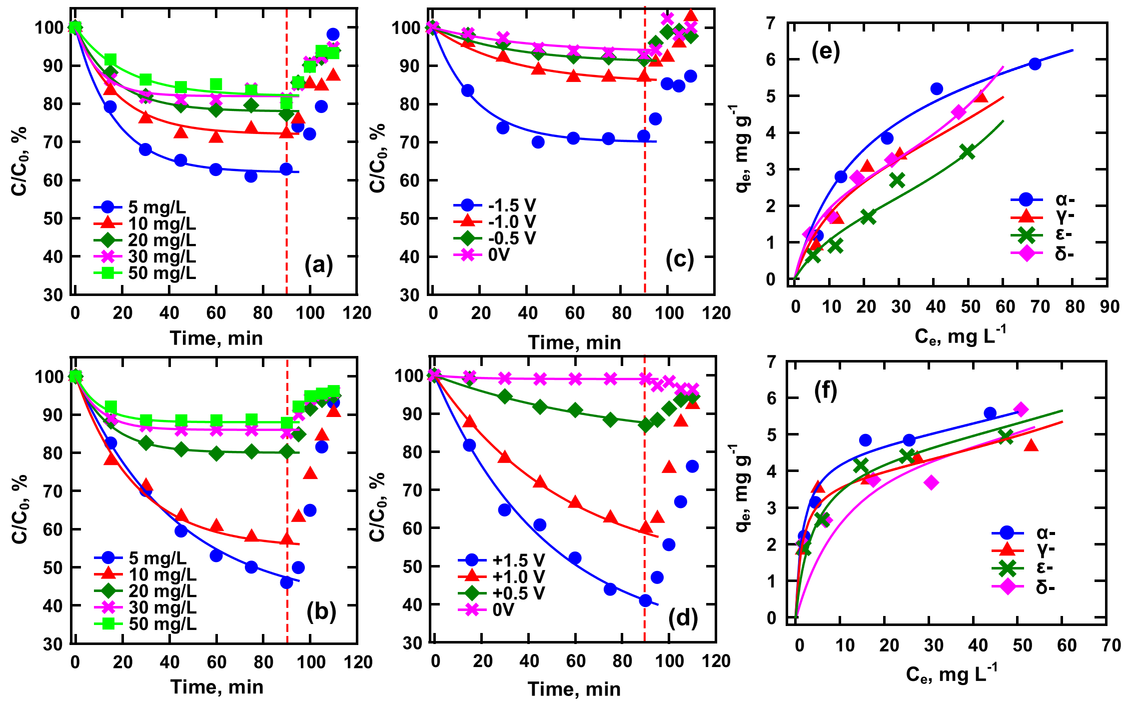

Fig. 4. Concentration changes of $NaNO_3$ electrosorption using αMnO_2/AC at different concentrations (NO_3^--N = 5 – 50 mg L^{-1}) for (a) Na^+, (b) NO_3^-, and working potentials (±1.5 V vs. Ag/AgCl, NO_3^--N = 10 mg L^{-1}) for (c) Na^+, (d) NO_3^-. Sorption isotherms of (e) Na^+ (E = -1.5 V) and (f) NO_3^- (E = +1.5 V) on MnO_2/AC electrodes.

Fig. S8, Supporting Information), are summarized in Table 1. Results revealed relatively increasing adsorption rate constants with respect to AC, for all cations and anions, due to the pseudocapacitive charging of α-MnO_2 compared to EDL charging of AC. Note that incorporation of MnO_2 into AC, i.e., αMnO_2/AC composite, did not change the pore size and surface area of AC significantly (3.5 nm and 801 m^2-g^{-1} for αMnO_2/AC versus 4.1 nm and 752 m^2-g^{-1} for AC) (Fig. 2d). The rate of ion transport in the porous surface of activated carbon governs the ion separation efficiency of a typical CDI process. A tunable ratio of meso to micropore has been found to critically influence the CDI capacity of AC electrodes due to solution conductivity [56,57]. This work, however, showed that more reversible diffusion-controlled current accounting for ion intercalation will aid in higher rate of ion uptake onto the pseudocapacitor regardless of pore properties.

Based on the equilibrium, C_e, and given initial, C_o, ion concentrations, it is possible to calculate the ion adsorption capacity, q_e, (mg g^{-1}) or Γ_e, (eq g^{-1}) according to the following equations:

$$q_e = \frac{(C_0 - C_e)}{m} \times \mathrm{V} \tag{8a}$$

Table 1
Rate constants k_1 of first-order modeling for electrosorption of Li_2SO_4 (3.5 × 10^{-4} M), $NaNO_3$ (1 × 10^{-3} M), and $Ca(ClO_4)_2$ (3.5 × 10^{-4} M) as affected by working potentials on AC and αMnO_2/AC electrodes.

	Working potential E, V							
	−1.5	−1.0	−0.5	0	0	+0.5	+1.0	+1.5
	k_1 (10^{-2} min^{-1}) for Li^+				k_1 (10^{-2} min^{-1}) for SO_4^{2-}			
AC	3.7	2.8	1.8	1.4	2.9	2.2	3.7	4.0
αMnO_2/AC	4.1	3.4	2.6	6.5	3.9	2.5	3.9	4.7
	k_1 (10^{-2} min^{-1}) for Na^+				k_1 (10^{-2} min^{-1}) for NO_3^-			
AC	4.7	3.7	2.9	4.5	4.8	2.3	2.9	4.9
αMnO_2/AC	6.0	5.2	3.1	6.6	5.2	2.9	3.7	6.2
	k_1 (10^{-2} min^{-1}) for Ca^{2+}				k_1 (10^{-2} min^{-1}) for ClO_4^-			
AC	2.5	2.1	0.9	1.7	2.5	1.3	1.6	1.9
αMnO_2/AC	3.4	2.6	1.5	5.2	3.3	1.3	1.8	2.7

or

$$\Gamma_e = \frac{z \times (C_0 - C_e)}{Mw} \times \frac{V}{m} \tag{8b}$$

where, V is the volume of reaction solution (250 mL); z represents the ion valence; Mw is the molecular weight; m is the effective mass of active materials on graphite as the current collector (g). Considering a multilayer adsorption, the total surface coverage (θ) in subsequent layers is [23,32]:

$$\theta = \frac{K_1 C_e}{(1 - K_1 C_e)(1 + (K_1 - K_2) C_e)} \tag{9a}$$

Then the equilibrium adsorption capacity, q_e or Γ_e, can be calculated using the following equations:

$$q_e = \frac{K_1 C_e q_1}{(1 - K_1 C_e)(1 + (K_1 - K_2) C_e)} \tag{9b}$$

or

$$\Gamma_e = \frac{K_1 C_e \Gamma_1}{(1 - K_1 C_e)(1 + (K_1 - K_2) C_e)} \tag{9c}$$

where C_e is the equilibrium ion concentration (mg L^{-1}); K_1 and K_2 are the equilibrium constant for the first and the subsequent layer adsorption (L mg^{-1}), respectively; q_1 and Γ_1, represent the monolayer electrosorption capacity in mg g^{-1} and eq g^{-1}, respectively. When the first layer adsorption becomes predominated, K_2 is negligible and Eq. (9b) evolves to a type-I Langmuir equation (i.e., $K_1 = K_L$ and $q_1 = q_m$, monolayer capacity). Fig. 4e & 4f compare adsorption isotherm of Na^+ and NO_3^- (at −1.5 V and + 1.5 V, respectively) on different MnO_2 polymorphs. The monolayer capacity, q_m, and adsorption constant, K_1, as well as the Gibbs free energy of adsorption calculated from the equilibrium constant, i.e., $\Delta G^0 = -2.303 \times RT \times \log K$ are listed in Table 2. Results showed that the adsorption energy of Na^+ was slightly smaller than that of NO_3^- and that the adsorption energy for second layer was one order of magnitude smaller than that of the first layer. As predicted by the

Table 2
Monolayer capacities and Langmuir constants of MnO_2/AC electrodes for electrosorption of $NaNO_3$.

	Na^+ (at −1.5 V vs. Ag/AgCl)					NO_3^- (at + 1.5 V vs. Ag/AgCl)				
	q_m mg-Na/g (10^{-4} mol/g)	K_1 10^{-2} L/mg-Na (10^3 L/mol)	$-\Delta G_1^0$ kJ/mol	K_2 10^{-2} L/mg (10^2 L/mol	$-\Delta G_2^0$ kJ/mol	q_m, mg-N/g (10^{-4} mol/g)	K_1 10^{-2} L/mg-N (10^3 L/mol	$-\Delta G_1^0$ kJ/mol	K_2 10^{-2} L/mg-N (10^2 L/mol)	$-\Delta G_2^0$ kJ/mol
α-MnO_2	6.2 (2.70)	5.8 (1.33)	17.83	0.2 (0.46)	9.49	4.6 (2.00)	62 (8.68)	22.47	0.4 (0.56)	9.97
γ-MnO_2	2.8 (1.22)	15 (3.45)	20.19	0.9 (2.07)	13.21	4.5 (1.96)	26 (3.64)	20.32	0.4 (0.56)	9.97
δ-MnO_2	3.6 (1.57)	8.0 (1.84)	18.63	0.6 (1.38)	12.21	3.0 (1.30)	72 (10.10)	22.84	0.9 (1.26)	11.98
ε-MnO_2	2.2 (0.96)	7.0 (1.61)	18.30	0.9 (2.07)	13.21	3.8 (1.65)	70 (9.80)	22.77	0.5 (0.70)	10.53

electrical capacitance, α-MnO_2 has the highest total ion adsorption capacity (q_m of Na^+ and NO_3^- = 6.2 and 4.6 mg g^{-1}, or 0.27 and 0.33 mmol/g, respectively) among the four crystal phases; notably, MnO_2, a pseudocapacitor, has rather different ion adsorption characteristics toward cationic and anionic electrolyte. Na^+ adsorption belonged to the type-II Langmuir adsorption isotherm (Fig. 4e), while that of NO_3^- was nearly fitted by a monolayer equation (Fig. 4f). Further, the bonding energy of NO_3^- was generally greater than that of Na^+, i.e., larger K_1 (Table 2). Since the surface charge originated from the redox reaction is supposed to be balanced by intercalation, MnO_2 surface was endowed with sites of different adsorption energy. Cations shall fill up the porous surfaces and penetrate deeper into the reduced Mn(III) tunnels.

Fig. 5 and Fig. 6 show the electrosorption isotherms of cations and anions of AC and αMnO_2/AC electrodes, respectively, under different working potentials. The Supporting Material (Fig. S3 to Fig. S8) gives the concentration profile of ions as a function of adsorption time at different applied potentials (-1.5 V to + 1.5 V, vs. Ag/AgCl), in which the equilibrium concentration, C_e (mol L^{-1}) was used to estimate the adsorption capacity, Γ_e (mol g^{-1}) and to construct the adsorption isotherm. As expected, the ion adsorption capacity increased with increasing working potential. Table 3 collects the Langmuir constant, K_1, and associated free energy of adsorption, ΔG_1^o, at different working potentials. The α-MnO_2/AC electrode exhibited relatively small K_1 value than that of AC electrode. (Note: This is a fortuitous situation as it will be easier for discharging the α-MnO_2/AC electrode.) The Type-II adsorption isotherm better described the ion adsorption characteristics of pseudocapacitor, i.e., α-MnO_2/AC electrode than that of EDL capacitor, particularly, at high electrode potential, considering the heterogeneity of the composite surface. The K_1 vale followed the order: Li^+ > Ca^{2+} > Na^+ for cations, and SO_4^{2-} > NO_3^- > ClO_4^- for anions. Results indicated the inertness characteristics of Na^+ and ClO_4^- (or affinity toward the electrode) relative to Li^+, Ca^{2+}, NO_3^- and SO_4^{2-}. Obviously, the ion solvation energy plays a role on it adsorption onto pseudocapacitor [58]. The hydration enthalpy for cation are 409, 519, and 1,577 kJ/mole for Na^+, Li^+ and Ca^{2+}, and for anions are 229, 314, and 1,059 kJ/mol, for ClO_4^-, NO_3^- and SO_4^{2-}, respectively [59]. Note that the hydration enthalpy is proportional

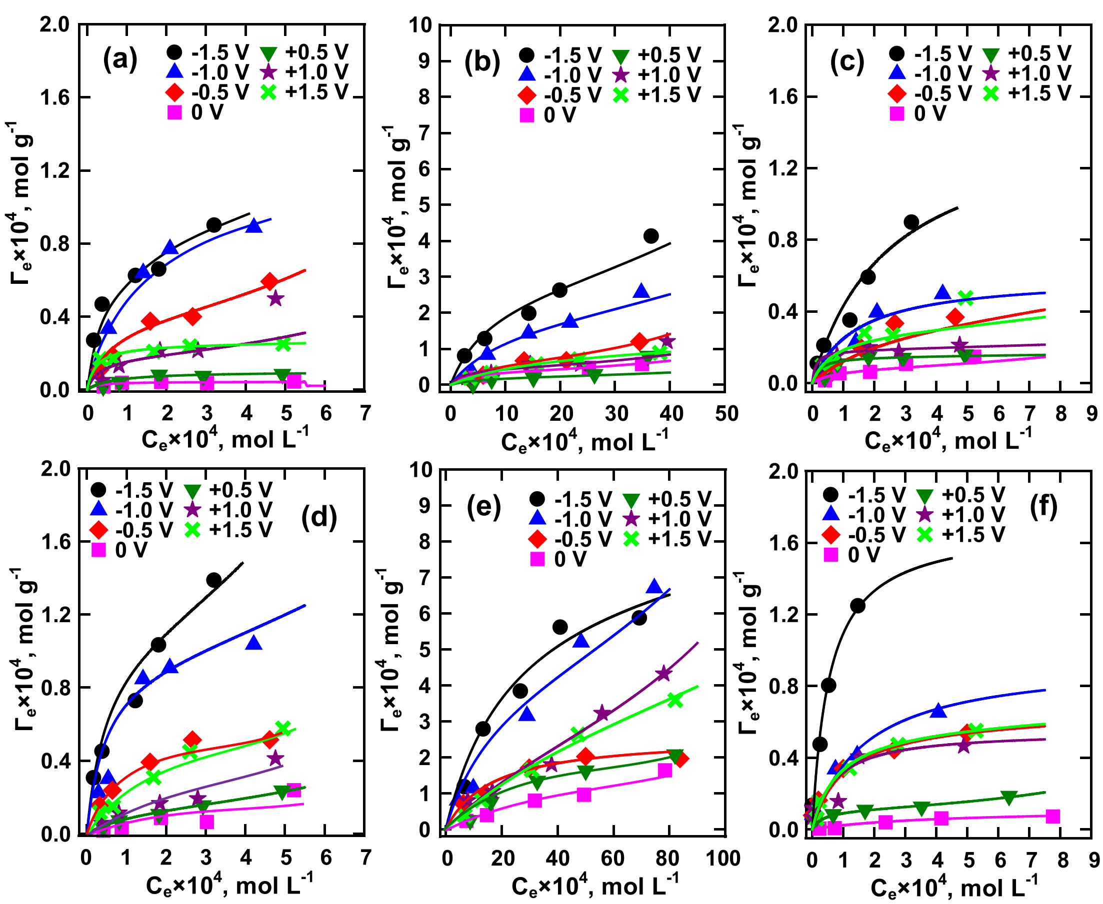

Fig. 5. Electrosorption isotherms of cations on AC: (a) Li^+, (b) Na^+, and (c) Ca^{2+}, and on αMnO_2/AC: (d) Li^+, (e) Na^+, and (f) Ca^{2+}, as affected by applied potentials (vs. Ag/AgCl).

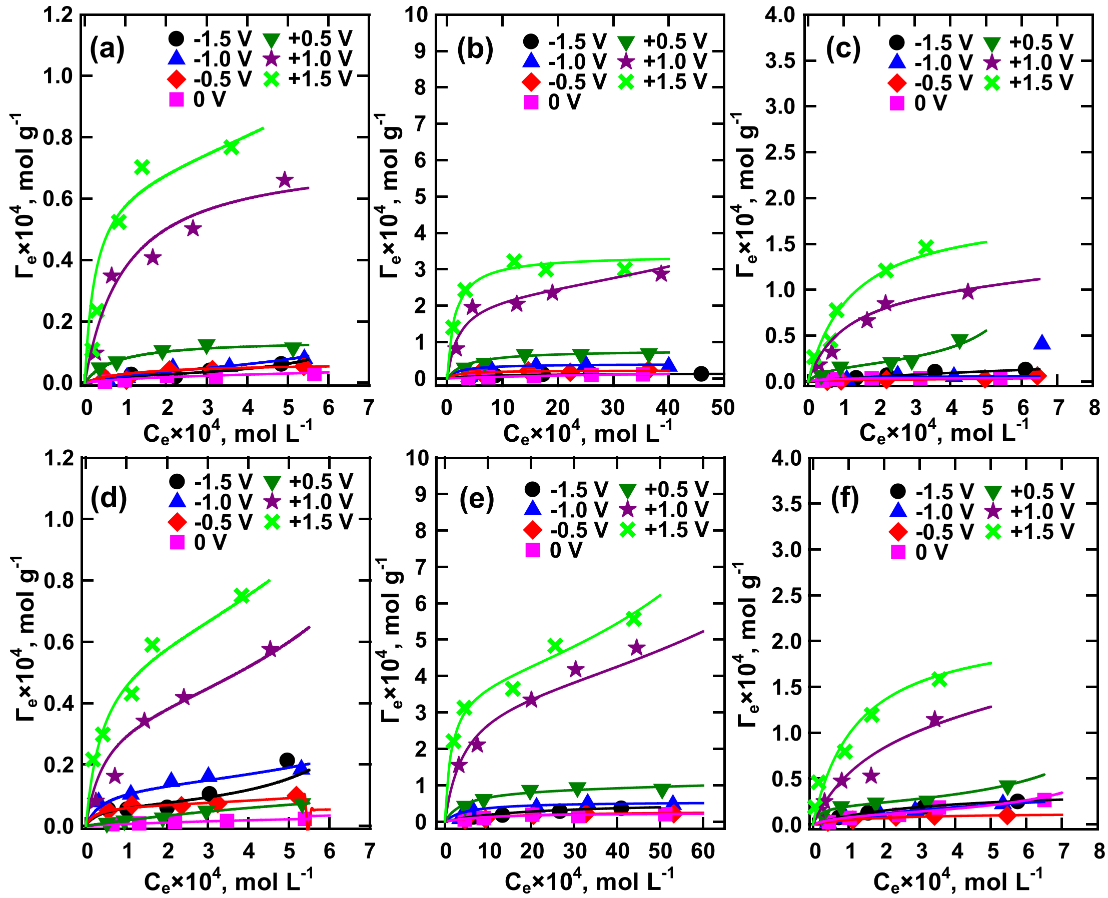

Fig. 6. Electrosorption isotherms of anions on AC: (a) SO_4^{2-}, (b) NO_3^-, and (c) ClO_4^-, and on αMnO_2/AC: (d) SO_4^{2-}, (e) NO_3^-, and (f) ClO_4^- at different applied potentials (vs. Ag/AgCl).

Table 3
Langmuir constants K_1 of Li_2SO_4, $NaNO_3$, and $Ca(ClO_4)_2$ on AC and αMnO_2/AC electrodes as afunction of applied potential (V vs. Ag/AgCl).

	Working potential E, V							
	−1.5	−1.0	−0.5	0	0	+0.5	+1.0	+1.5
	K_1 (L mmol^{-1})/-ΔG_1^0 (kJ/mol) for Li^+				K_1 (L mmol^{-1})/-ΔG_1^0 (kJ/mol) for SO_4^{2-}			
AC	4.50/12.5	1.89/5.29	1.73/4.56	0.51/-5.60	0.62/-3.98	1.31/2.25	1.62/4.01	4.0/11.5
αMnO_2/AC	1.22/1.65	1.55/3.64	1.62/4.01	0.42/-7.21	0.25/-11.5	1.29/2.21	1.21/1.59	1.8/4.89
	K_1 (L mmol^{-1})/-ΔG_1^0 (kJ/mol) for Na^+				K_1 (L mmol^{-1})/-ΔG_1^0 (kJ/mol) for NO_3^-			
AC	0.14/-16.6	0.13/-16.9	0.17/-14.7	0.38/-8.05	0.02/–33.4	0.27/-10.9	0.47/-6.28	0.72/-2.73
αMnO_2/AC	0.05/-24.9	0.03/-28.6	0.06/–23.4	0.15/-15.8	0.12/-17.6	0.18/-14.3	0.38/-8.05	0.51/-5.6
	K_1 (L mmol^{-1})/-ΔG_1^0 (kJ/mol) for Ca^{2+}				K_1 (L mmol^{-1})/-ΔG_1^0 (kJ/mol) for ClO_4^-			
AC	1.35/2.5	0.64/-3.71	0.85/-1.35	0.28/-10.6	0.42–7.21	0.93/-0.6	1.14/1.09	1.82/4.98
αMnO_2/AC	0.68/-3.21	0.55/-4.97	0.42/-7.21	0.51/-5.6	0.55/-4.97	0.62/-3.98	1.05/0.41	1.07/0.56

to the square of ionic charge and reciprocally proportional to the Pauling crystal radius [60]. Increasing hydration enthalpy tends to facilitate ion adsorption on pseudocapacitive charging over that of activated carbon.

Results of the monolayer ion adsorption capacity (Γ_m, in eq. g^{-1}) in Figs. 5 & 6 were plotted as a function of applied potential as shown in Fig. 7a to c. Contrast to the AC electrode, clearly, decoration of α-MnO_2 on AC enhanced the adsorption of cations studied. The result affirmed the beneficial effect of pseudocapacitance due to increase in surface ion conductivity because of cation intercalation. That is, the presence of Mn (III) on MnO_2 structure creates negatively charged surface sites that promotes cation adsorption, but not anions. At −1.5 V, the adsorption capacity of AC for Na^+, Ca^{2+}, and Li^+ were 2.8 × 10^{-4}, 2.1 × 10^{-4} , and 0.76 × 10^{-4} mol g^{-1}, respectively, which were increased to 5.1 × 10^{-4} , 4.0 × 10^{-4} , and 1.3 × 10^{-4} mol g^{-1}, respectively, on α-MnO_2/AC. At + 1.5 V. Whereas, there is not much difference between AC and α-MnO_2/AC on anion adsorption capacity; the adsorption capacity of AC for NO_3^-, ClO_4^-, and SO_4^{2-} were 3.5 × 10^{-4}, 1.5 × 10^{-4}, and 1.3 × 10^{-4} mol g^{-1}, respectively; and those of α-MnO_2/AC were 3.0 × 10^{-4}, 1.9 × 10^{-4}, and 1.2 × 10^{-4} mol g^{-1}, respectively. The cation electrosorption capacity followed the order: $Na^+ > Ca^{2+} > Li^+$, which could be attributed to the ion valence and effective radius (i.e., hydration energy). At the vicinity of an electrical double layer, the hydration sphere surrounding an ion is electrostatically adsorbed at the Stern plane, so that the columbic interaction becomes stronger as the ions with higher charges and smaller radius are stored [60]. Note that the size of hydrated cations are Ca^{2+} (4.12 Å) > Li^+ (3.82 Å) > Na^+ (3.58 Å) [21] and the enthalpy was Ca^{2+} (1,577 kJ/mol) > Li^+ (519 kJ/mol) > Na^+ (409 kJ/mol) [59]. For smooth surface, divalent ions are much favored than monovalent ions; whereas it is not completely true when the surface structure is porous [61]. The adsorption capacity of oxyanions followed the order: NO_3^- >

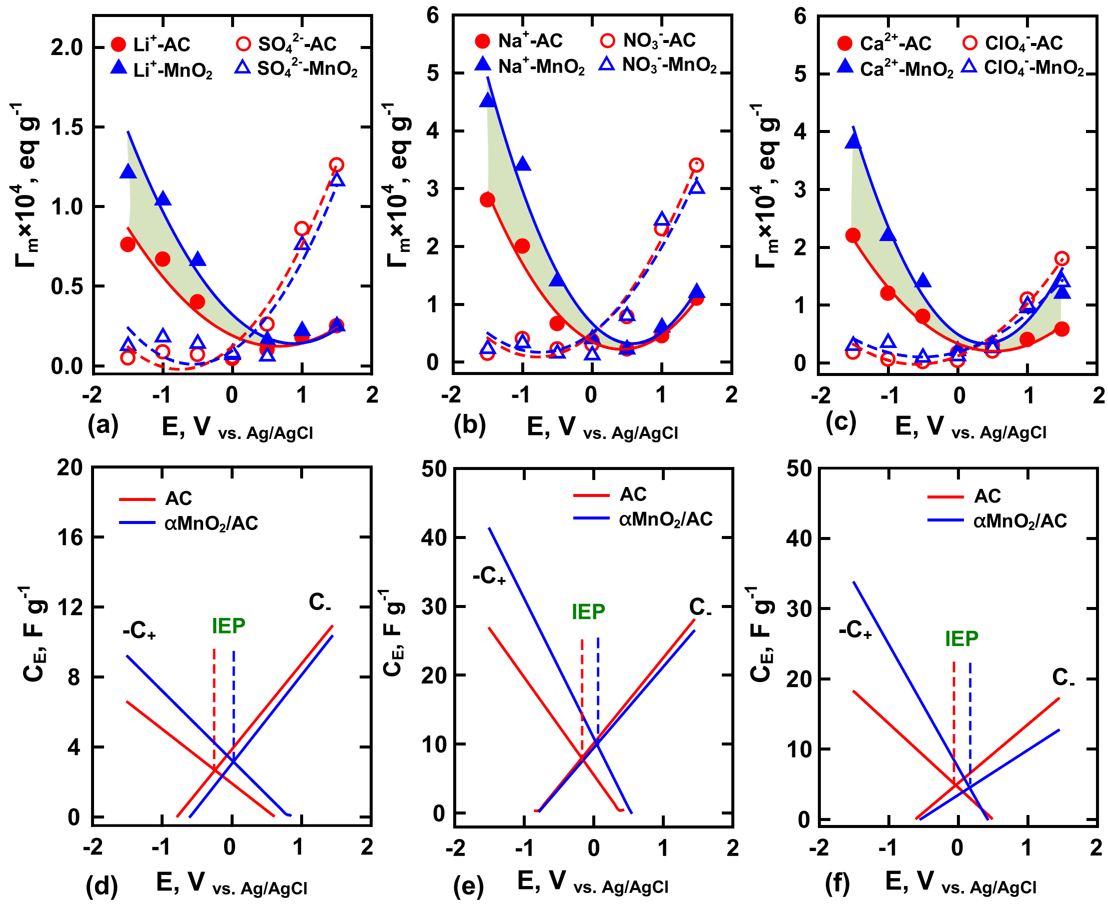

Fig. 7. Monolayer capacities of AC and αMnO_2/AC electrodes for electrosorption of (a) Li_2SO_4, (b) $NaNO_3$, and (c) $Ca(ClO_4)_2$; electrical capacitances in the presence of (a) Li_2SO_4, (b) $NaNO_3$, and (c) $Ca(ClO_4)_2$ as a function of applied potentials (vs. Ag/AgCl).

$ClO_4^- > SO_4^{2-}$, which suggests that the hydrated radius and thus hydration energy is determining factor, that is, ClO_4^- (3.8 Å) ~ SO_4^{2-} (3.79 Å) > NO_3^- (3.35 Å) and ClO_4^- (229 kJ mol^{-1}) < NO_3^- (314 kJ mol^{-1}) < SO_4^{2-} (1,059 kJ mol^{-1}) [53]. However, the large difference between sorption of ClO_4^- and SO_4^{2-} can be attributed to the Pauling's electronegativity that are in descending order: ClO_4^- (5.43) > NO_3^- (4.32) > SO_4^{2-} (2.74), in the three anion groups [62,63]. Effects of electronegativity significantly on the selectivity at specific anode potentials of CDI have been reported; anions of a larger electronegativity are preferentially removed [64].

Moreover, the monolayer surface excess of inert electrolyte, Γ, can be related to surface charge, σ, i.e., $\sigma_+ \equiv F\Gamma_+$ and $\sigma_- \equiv F\Gamma_-$. Hence, the differential capacitance can be subdivided into that due to cations, $C_{E,+}$ and that due to anions, $C_{E,-}$ by defining:

$$C_{E,+} = -\frac{\partial \sigma_+}{\partial E} = -\frac{F\partial \Gamma_{m,+}}{\partial \Psi} \tag{10a}$$

and

$$C_{E,-} = -\frac{\partial \sigma_-}{\partial E} = -\frac{F\partial \Gamma_{m,-}}{\partial \Psi} \tag{10b}$$

where Ψ is the potential of the polarized electrode. The computed componential capacitance, C_E, of AC and α-MnO_2/AC electrode are shown in Fig. 7d to f. Note that $C_{E,+}$ and $C_{E,-}$ are generally symmetrical for the AC electrode. By comparison, as surface potential was rendered more negative, the increase in $C_{E,+}$ of α-MnO_2/AC was steeper than that of AC, indicating that cations were more favorably adsorbed by MnO_2 surface than anions. According to the Lipmann theory, at the potential of isoelectric point (IEP), or the electrocapillary maximum, the capacitance $C_{E,+}$ will be equal but opposite in sign to $C_{E,-}$ and the surface carries zero net electrical charge. For all electrolytes studied, the IEP of α-MnO_2/AC was around + 30 mV greater than that of AC. As a reversible surface, such as MnO_2, the surface potential can be modified also by the solution pH; that is, H^+ and OH^- are the potential-determining ions. Ideally the surface potential, Ψ_o, is a function of pH and pH_{zpc}, $\Psi_o = -0.059\times(pH-pH_{zpc})$, according the Nernst equation, where pH_{zpc} is the pH at the zero-point of charge. Upon charging or discharging the surface, the total capacitance, C_E, is therefore the sum of reversible (pH controlled) and polarizable (E controlled) capacitors in parallel. The distribution of surface hydroxyl species, ($\underline{S}$-O^- or $\underline{S}$–OH_2^+) is dependent on the activity of potential determining ions, i.e., H^+ and OH^-, and contributes to the polarity of electrosorption. Fig. S9 (Supporting Materials) shows that the pH_{pzc} of all MnO_2 polymorphs (<4) were smaller than that of AC (pH_{pzc} = 6). Although the controlled solution pH slightly changed during electrosorption, that is, based on electroneutrality pH would decrease and increase via sorption of cation and anion, respectively. Fig. 8 illustrates the mechanism of ions storage in pseudocapacitor in terms of charge accumulation over reversible and polarizable surfaces at different degrees of surface polarization, namely, zero (left), cathodic (middle) and anodic (right) potentials, respectively. In summary, an asymmetric electrode, α-MnO_2/AC had more negative charge sites than AC over a wide pH range. The nature of surface ionic group on the hydrous solid, therefore, led to a positive shift in IEP after loading with MnO_2 on AC, which as a result, more positive potential shall be applied as to reach a point of zero net charge where -$C_{E,+}$ = $C_{E,-}$. Such an effect must largely be related to CDI system capable of accommodating more cations on pseudocapacitor, i.e., α-MnO_2/AC than on EDL capacitor, i.e., AC.

In practical application, the CDI electrode can be repeatedly run for

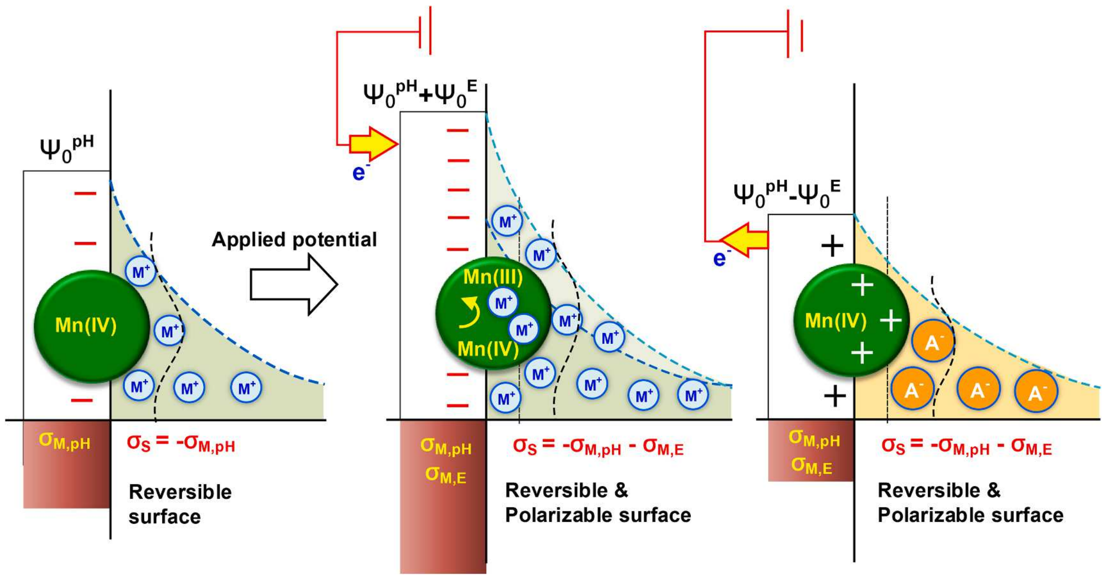

Fig. 8. Mechanism of ion storage in MnO_2/AC electrode at different degrees of surface polarization.

sorption and desorption of ions in the waste stream by applying a specific voltage drop (charging) or zero (discharging) voltage, respectively. We provided a cycle test for sorption of $NaNO_3$ using αMnO_2/AC electrode as shown in Fig. S10. The electrode did not significantly degrade at least in five sorption–desorption runs. Further management of salt concentrate from CDI unit was determined by the quality of the concentrated stream. Established technology, such as RO, IER, EDR, has been suggested as post-treatment of desalination concentrate in terms of thermal, crystallization or membrane processes [65,66].

Table 4 gathers salt and ion adsorption capacity (meq g^{-1}) of biomass-derived CDI electrodes reported recently. The AC precursors were waste cellulose [67], rice [68,69], fruit shell [70-73], and vegetables [74-77], in which the desalination efficiency and adsorption capacity for NaCl were obtained at a constant voltage drop ($\Delta V = 1.2$ V). The carbon-based pseudocapacitor for the removal of common ions other than Na^+ or salts other than NaCl was rarely investigated. The present work provided the ion adsorption capacity of αMnO_2/AC under specific working potentials (E_{app}); the loaded manganese oxide particularly enhanced the cation uptake compared to the carbon (EDL) electrode. Note that most authors determined CDI capacity by integration of the CV curve or conductivity measurement. These methods do not reflect accurately the ion adsorption capacity. The CV curve method overestimates the deionization capacity, whereas the conductivity method assumes equal sorption capacity toward Na^+ and Cl^- ion in the case of CDI removal of NaCl salt. Based on Table 4, the Na^+ adsorption capacity followed the order: coconut shell (1.47 meq-g^{-1}) > bacterial cellulose

Table 4
Summary of biomass precursors for CDI electrodes in the removal of common ions.

Biomass	Preparation	Characteristics	Electrochemical properties	Ref.
Bacterial-cellulose	Carbonized at 700 °C with N_2 and He gas for rGO/AC	BET = 340 m^2/g C_d = 366F/g	Capacity at ΔV = 1.2 V for NaCl = 1.88 meq-g^{-1}	[67]
Rice husk	Activated at 800 °C with KOH	BET = 1839 m^2/g Pore size = 3.8 nm C_d = 120.5F/g	Capacity at ΔV = 1.2 V for NH_4^+ = 0.09 meq-g^{-1}; Mg^{2+} = 0.13 meq-g^{-1}; Cu^{2+} =0.02 meq-g^{-1}	[68]
Rice husk	Carbonized at 750 °C;Activated at 800 °C with NaOH	BET = 1638 m^2/g Pore size = 0.83 nm C_d = 91F/g	Capacity at ΔV = 1.2 V for NaCl = 0.53 meq-g^{-1}	[69]
Almond shell	Carbonized and activated at 900 °C with CO_2	BET = 450 m^2/g Pore size = 3.8 nm	Capacity at ΔV = 1.2 V for NaCl = 0.66 meq-g^{-1}	[70]
Tamarind shell	Carbonized at 350 °C;Activated at 800 °C with KOH and urea for N-doped AC	BET = 410 m^2/g Pore size = 3.87 nm C_d = 174.5F/g	Capacity at ΔV = 1.2 V for NaCl = 0.64 meq-g^{-1}	[71]
Peanut shell	Activated at 500 °C with H_3PO_4; hydrothermal deposition of $FeCl_2$/$FeCl_3$ for Fe_3O_4/PSAC	BET = 525 m^2/g Pore size = 1.7 nm C_d = 307F/g	Capacity at ΔV = 1.2 V for Cr(VI) = 2.83 meq-g^{-1}	[72]
Coconut shell	Carbonized at 500 °C; activated with KOH at 675 °C; precipitation of $KMnO_4$ for synthesis of AB-MnO_2/AC	BET = 304 m^2/g C_d = 523F/g	Capacity at ΔV = 1.2 V for Na^+ = 1.47 meq-g^{-1}	[73]
Palm leaflets	Carbonized at 500 °C;Activated at 700 °C with NaOH	BET = 604 m^2/g C_d = 23.3F/g	Capacity at ΔV = 1.2 V for NaCl = 0.18 meq-g^{-1}	[74]
Sorghum	Carbonized at 800 °C; activated with KOH at 800 °C	BET = 1347 m^2/g C_d = 257F/g	Capacity at ΔV = 1.2 V for NaCl = 1.00 meq-g^{-1}	[75]
Watermelon rind	Activated at 500 °C with H_3PO_4; hydrothermal deposition of Mn(II)/Fe(III) for $MnFe_2O_4$/WMAC	BET = 483 m^2/g Pore size = 3.7 nm C_d = 425F/g	Capacity at ΔV = 1.2 V for NaCl = 1.02 meq-g^{-1}	[76]
Artocarpus heterophyllus peels	Carbonized at 400 °C; activated with KOH at 600 °C	BET = 607 m^2/g Pore size = 3.05 nm C_d = 610F/g	Capacity at ΔV = 2 V for NaCl = 0.20 meq-g^{-1}	[77]
Loofah	Activated at 800 °C with $ZnCl_2$; precipitation of $KMnO_4$ for synthesis of αMnO_2/AC	BET = 801 m^2/g Pore size = 3.5 nm C_d = 75F/g	Capacity at E_{app} = +1.5 V for SO_4^{2-} = 0.46 meq-g^{-1}; NO_3^- = 0.3 meq-g^{-1}; ClO_4^- = 0.14 meq-g^{-1}; Li^+ = 0.12 meq-g^{-1}; Na^+ = 0.45 meq-g^{-1}; Ca^{2+} = 1.52 meq-g^{-1}	This work

(0.94 meq-g^{-1}) > watermelon rind (0.51 meq-g^{-1}) > sorghum (0.50 meq-g^{-1}) > loofah (0.45 meq-g^{-1}) > almond shell (0.33 meq-g^{-1}) > tamarins shell (0.32 meq-g^{-1}) > rice husk (0.26 meq-g^{-1}) > artocarpus heterophyllus peels (0.10 meq-g^{-1}) > palm leaflet (0.09 meq-g^{-1}).

4. Conclusion

The pseudocapacitance at the interface of MnO_2 supported on a loofah-derived activated carbon in the presence of common water electrolytes, including $NaNO_3$, Li_2SO_4, and $Ca(ClO_4)_2$, were investigated in constant potential mode (vs. Ag/AgCl). Among all four polymorphs studied, α-MnO_2 was the best pseudocapacitor with respect to ion adsorption capacity readily described by the modified Langmuir adsorption isotherm. Results indicated that there was insignificant difference in BET surface area between AC (752 m^2 g^{-1}) and αMnO_2/AC composite (801 m^2 g^{-1}). However, loading of MnO_2 on AC increased significantly the first-order ion electrosorption rate constant and monolayer ion adsorption capacity of AC in the presence of common inert electrolytes due to improvement in diffusion-controlled capacitance. The mechanism of ion intercalation mainly aided in cation adsorption at negatively polarized electrode. Hence, the effective radius and valence that influenced the ion solvation (i.e., energy of hydration) of ions, played a significant role on the removal efficiency of ions. The adsorption capacity of αMnO_2/AC toward cations studied was in the order of Na^+ (2.8×10^{-4} mol g^{-1}) > Ca^{2+} (2.1×10^{-4} mol g^{-1}) > Li^+ (0.76×10^{-4} mol g^{-1}), at a working potential of −1.5 V (vs. Ag/AgCl). The isoelectric point (IEP) of the α-MnO_2/AC electrode shifted toward more positively polarized potential relative to that of the AC electrode. At IEP, i.e., the point of zero net charge, the differential capacitance contributed by cations and anions was equal.

Declaration of Competing Interest

The authors declare that they have no known competing financial interests or personal relationships that could have appeared to influence the work reported in this paper.

Acknowledgements

The authors would like to thank the Ministry of Science and Technology, Taiwan for generous finance support of this research project under Contract No. MOST 107-2221-E-110 -001 -MY3. Additional support was provided by NSF by US NSF IOA through grant no. 1632899 to CPH.

Appendix A. Supplementary data

Supplementary data to this article can be found online at https://doi.org/10.1016/j.cej.2021.130606.

References

[1] M.A. Alaei Shahmirzadi, S.S. Hosseini, J. Luo, I. Ortiz, Significance, evolution and recent advances in adsorption technology, materials and processes for desalination, water softening and salt removal, J. Environ. Manag. 215 (2018) 324–344.

[2] T. Mezher, H. Fath, Z. Abbas, A. Khaled, Techno-economic assessment and environmental impacts of desalination technologies, Desalination 266 (1-3) (2011) 263–273, https://doi.org/10.1016/j.desal.2010.08.035.

[3] I. Ihsanullah, M.A. Atieh, M. Sajid, M.K. Nazal, Desalination and environment: A critical analysis of impacts, mitigation strategies, and greener desalination technologies, Sci. Total Environ. 780 (2021) 146585, https://doi.org/10.1016/j.scitotenv.2021.146585.

[4] A.S. Alsaman, A.A. Askalany, K. Harby, M.S. Ahmed, A state of the art of hybrid adsorption desalination–cooling systems, Renew. Sustain. Energ. Rev. 58 (2016) 692–703, https://doi.org/10.1016/j.rser.2015.12.266.

[5] A.M. Abioye, F.N. Ani, Recent development in the production of activated carbon electrodes from agricultural waste biomass for supercapacitors: A review, Renew. Sustain. Energ. Rev. 52 (2015) 1282–1293, https://doi.org/10.1016/j.rser.2015.07.129.

[6] J. Choi, P. Dorji, H.K. Shon, S. Hong, Applications of capacitive deionization: Desalination, softening, selective removal, and energy efficiency, Desalination 449 (2019) 118–130, https://doi.org/10.1016/j.desal.2018.10.013.

[7] N. Lee, M.-L. Liu, M.-C. Wu, T.-H. Chen, C.-H. Hou, The effect of redox potential on the removal characteristic of divalent cations during activated carbon-based capacitive deionization, Chemosphere 274 (2021) 129762, https://doi.org/10.1016/j.chemosphere.2021.129762.

[8] P. Liu, T. Yan, J. Zhang, L. Shi, D. Zhang, Separation and recovery of heavy metal ions and salt ions from wastewater by 3D graphene-based asymmetric electrodes: via capacitive deionization, J. Mater. Chem. A. 5 (28) (2017) 14748–14757, https://doi.org/10.1039/C7TA03515B.

[9] A. Kalfa, B. Shapira, A. Shopin, I. Cohen, E. Avraham, D. Aurbach, Capacitive deionization for wastewater treatment: Opportunities and challenges, Chemosphere 241 (2020) 125003, https://doi.org/10.1016/j.chemosphere.2019.125003.

[10] A.G. El-Deen, N.A. Barakat, K.A. Khalil, M. Motlak, H.Y. Kim, Graphene/SnO_2 nanocomposite as an effective electrode material for saline water desalination using capacitive deionization, Ceram. Int. 40 (9) (2014) 14627–14634, https://doi.org/10.1016/j.ceramint.2014.06.049.

[11] A.G. El-Deen, J.H. Choi, C.S. Kim, K.A. Khalil, A.A. Almajid, N.A. Barakat, TiO_2 nanorod-intercalated reduced graphene oxide as high performance electrode material for membrane capacitive deionization, Desalination 361 (2015) 53–64, https://doi.org/10.1016/j.desal.2015.01.033.

[12] C. Zhang, S. Bhoyate, C. Zhao, P. Kahol, N. Kostoglou, C. Mitterer, S. Hinder, M. Baker, G. Constantinides, K. Polychronopoulou, C. Rebholz, R. Gupta, Electrodeposited nanostructured $CoFe_2O_4$ for overall water splitting and supercapacitor applications, Catalysts 9 (2) (2019) 176, https://doi.org/10.3390/catal9020176.

[13] R.R. Maça, D. Címtora Juárez, M. Castillo Rodríguez, V. Etacheri, Nanointerface-driven pseudocapacitance tuning of TiO_2 nanosheet anodes for high-rate, ultralong-life and enhanced capacity sodium-ion batteries, Chem. Eng. J. 391 (2020) 123598, https://doi.org/10.1016/j.cej.2019.123598.

[14] J.K. Seo, JaeWook Shin, H. Chung, P.Y. Meng, X. Wang, Y.S. Meng, Intercalation and Conversion Reactions of Nanosized β-MnO_2 Cathode in the Secondary Zn/MnO_2 Alkaline Battery, J. Phys. Chem. C 122 (21) (2018) 11177–11185, https://doi.org/10.1021/acs.jpcc.7b1168510.1021/acs.jpcc.7b11685.s001.

[15] A. Gambou-Bosca, D. Bélanger, Effect of the formulation of the electrode on the pore texture and electrochemical performance of the manganese dioxide-based electrode for application in a hybrid electrochemical capacitor, J. Mater. Chem. A 2 (2014) 6463–6473, https://doi.org/10.1039/C3TA14910B.

[16] C.M. Julien, M. Massot, C. Poinsignon, Lattice vibrations of manganese oxides. Part I. Periodic structures, Spectrochim. Acta A 60(3) (2004), 689-700, https://doi.org/10.1016/S1386-1425(03)00279-8.

[17] J. Elisadiki, C.K. King'ondu, Performance of ion intercalation materials in capacitive deionization/electrochemical deionization: A review, J. Electroanal. Chem. 878 (2020) 114588, https://doi.org/10.1016/j.jelechem.2020.114588.

[18] S. Vafakhah, Z. Beiramzadeh, M. Saeedikhani, H.Y. Yang, A review on free-standing electrodes for energy-effective desalination: Recent advances and perspectives in capacitive deionization, Desalination 493 (2020) 114662, https://doi.org/10.1016/j.desal.2020.114662.

[19] A. Carmona-Orbezo, R.A.W. Dryfe, Understanding the performance of flow-electrodes for capacitive deionization through hydrodynamic voltammetry, Chem. Eng. J 406 (2021) 126826, https://doi.org/10.1016/j.cej.2020.126826.

[20] S. Porada, R. Zhao, A. van der Wal, V. Presser, P.M. Biesheuvel, Review on the science and technology of water desalination by capacitive deionization, Prog. Mater. Sci. 58 (8) (2013) 1388–1442, https://doi.org/10.1016/j.pmatsci.2013.03.005.

[21] J. Oladunni, J. Zain, A. Hai, F. Banat, G. Bharath, E. Alhseinat, A Comprehensive review on recently developed carbon based nanocomposites for capacitive deionization: from theory to practice, Sep. Purif. Technol. 207 (2018) 291–320, https://doi.org/10.1016/j.seppur.2018.06.046.

[22] O. Pastushok, F. Zhao, D.L. Ramasamy, M. Sillanpää, Nitrate removal and recovery by capacitive deionization (CDI), Chem. Eng. J. 375 (2019) 121943, https://doi.org/10.1016/j.cej.2019.121943.

[23] Y.J. Shih, C.D. Dong, Y.H. Huang, C.P. Huang, Electro-sorption of ammonium ion onto nickel foam supported highly microporous activated carbon prepared from agricultural residues (dried *Luffa cylindrica*), Sci. Total Environ. 673 (2019) 296–305, https://doi.org/10.1016/j.scitotenv.2019.04.066.

[24] Y.-H. Tu, Y.-H. Yang, C.-C. Hu, A highly efficient faradaic desalination system utilizing MnO_2 and polypyrrole-coated titanium electrodes, Desalination 498 (2021) 114807, https://doi.org/10.1016/j.desal.2020.114807.

[25] Y. Liu, X. Gao, L.u. Zhang, X. Shen, X. Du, X. Dou, X. Yuan, Mn_2O_3 nanoflower decorated electrospun carbon nanofibers for efficient hybrid capacitive deionization, Desalination 494 (2020) 114665, https://doi.org/10.1016/j.desal.2020.114665.

[26] R.L. Zornitta, L.A.M. Ruotolo, Simultaneous analysis of electrosorption capacity and kinetics for CDI desalination using different electrode configurations, Chem. Eng. J. 332 (2018) 33–41, https://doi.org/10.1016/j.cej.2017.09.067.

[27] Y.-J. Peng, T.-H. Wu, C.-T. Hsu, S.-M. Li, M.-G. Chen, C.-C. Hu, Electrochemical characteristics of the reduced graphene oxide/carbon nanotube/polypyrrole composites for aqueous asymmetric supercapacitors, J. Power Source. 272 (2014) 970–978.

[28] B. Chen, Y. Wang, Z. Chang, X. Wang, M. Li, X. Liu, L. Zhang, Y. Wu, Enhanced capacitive desalination of MnO_2 by forming composite with multi-walled carbon nanotubes, RSC Adv. 6 (8) (2016) 6730–6736, https://doi.org/10.1039/C5RA26210K.

[29] X. Gao, A. Omosebi, J. Landon, K. Liu, Enhanced salt removal in an inverted capacitive deionization cell using amine modified microporous carbon cathodes, Environ. Sci. Technol. 49 (18) (2015) 10920–10926, https://doi.org/10.1021/acs.est.5b02320.

[30] O. Sufiani, H. Tanaka, K. Teshima, R.L. Machunda, Y.A.C. Jande, Enhanced electrosorption capacity of activated carbon electrodes for deionized water production through capacitive deionization, Sep. Purif. Technol. 247 (2020) 116998, https://doi.org/10.1016/j.seppur.2020.116998.

[31] K. Hojo, T. Takahashi, K. Oshima, T. Haji, Y. Terayama, H. Matsumoto, S. Satokawa, Enhancement of ionic conductivity of aqueous solution by silanol groups over zeolite surface, Micropo. Mesopor. Mater. 312 (2021) 110743, https://doi.org/10.1016/j.micromeso.2020.110743.

[32] Y.-J. Shih, C.-D. Dong, Y.-H. Huang, C.P. Huang, Loofah-derived activated carbon supported on nickel foam (AC/Ni) electrodes for the electro-sorption of ammonium ion from aqueous solutions, Chemosphere 242 (2020) 125259, https://doi.org/10.1016/j.chemosphere.2019.125259.

[33] J. Yang, L. Zou, H. Song, Z. Hao, Development of novel MnO_2/nanoporous carbon composite electrodes in capacitive deionization technology, Desalination 276 (1-3) (2011) 199–206, https://doi.org/10.1016/j.desal.2011.03.044.

[34] P.-C. Li, C.-C. Hu, T.-C. Lee, W.-S. Chang, T.H. Wang, Synthesis and characterization of carbon black/manganese oxide air cathodes for zinc–air batteries: Effects of the crystalline structure of manganese oxides, J. Power Source. 269 (2014) 88–97, https://doi.org/10.1016/j.jpowsour.2014.06.108.

[35] Y.J. Shih, R.L. Huang, Y.H. Huang, Adsorptive removal of arsenic using a novel akhtenskite coated waste Goethite, J. Clean. Prod. 87 (2015) 897–905, https://doi.org/10.1016/j.jclepro.2014.10.065.

[36] F.W. Boyom-Tatchemo, F. Devred, G. Ndiffo-Yemeli, S. Laminsi, E.M. Gaigneaux, Plasma-induced redox reactions synthesis of nanosizedα-, γ- andδ-Mn_O2catalysts for dye degradation, Appl. Catal. B-Environ. 260 (2020), 118159, https://doi.org/10.1016/j.apcatb.2019.11.

[37] M.T.N. Dinh, C.C. Nguyen, T.L.T. Vu, V.T. Ho, Q.D. Truong, Tailoring porous structure, reducibility and Mn^{4+} fraction of ε-MnO_2 microcubes for the complete oxidation of toluene, Appl. Catal.-A 595 (2020), 117473, https://doi.org/10.1016/j.apcata.202.

[38] T. Gopi, G. Swetha, S.C. Shekar, C. Ramakrishna, B. Saini, R. Krishna, P.V.L. Rao, Catalytic decomposition of ozone on nanostructured potassium and proton containing δ-MnO_2 catalysts, Catal. Commun. 92 (2017) 51–55, https://doi.org/10.1016/j.catcom.2017.01.002.

[39] P. Samanta, S. Ghosh, P. Samanta, N.C. Murmu, T. Kuila, Alteration in capacitive performance of Sn-decorated MnO_2 with different crystal structure: An investigation towards the development of high-performance supercapacitor electrode materials, J. Energ. Storag. 28 (2020) 101281, https://doi.org/10.1016/j.est.2020.101281.

[40] V. Sahu, M. Mishra, G. Gupta, G. Singh, R.K. Sharma, Turning Hazardous Diesel Soot into High Performance Carbon/MnO_2 Supercapacitive Energy Storage Material, ACS Sustainable Chem. Eng. 5 (1) (2017) 450–459, https://doi.org/10.1021/acssuschemeng.6b0178810.1021/acssuschemeng.6b01788.s001.

[41] S.H. Kim, B.C. Park, Y.S. Jeon, Y.K. Kim, MnO_2 Nanowire−CeO_2 nanoparticle composite catalysts for the selective catalytic reduction of NOx with NH_3, ACS Appl. Mater. Interfaces 10 (38) (2018) 32112–32119, https://doi.org/10.1021/acsami.8b0960510.1021/acsami.8b09605.s001.

[42] C. Rogier, G. Pognon, P. Bondavalli, C. Galindo, G.T.M. Nguyen, C. Vancaeyzeele, P.H. Aubert, Electrodeposition of MnO_2 on spray-coated nanostructured carbon framework as high performance material for energy storage, Surf. Coat. Technol. 384 (2020) 12531, https://doi.org/10.1016/j.surfcoat.2019.125310.

[43] K.M. Racik, A. Manikandan, M. Mahendiran, P. Prabakaran, J. Madhavan, M.V. A. Raj, Fabrication of manganese oxide decorated copper oxide (MnO_2/CuO) nanocomposite electrodes for energy storage supercapacitor devices, Phys. E: Low-dimensional Syst. Nanostru. 119 (2020) 11403, https://doi.org/10.1016/j.physe.2020.114033.

[44] T.E. Kibona, G.N. Shao, H.T. Kim, C.K. King'ondu, Specific capacitance–pore texture relationship of biogas slurry mesoporous carbon/MnO2 composite electrodes for supercapacitors, Nano-Structures & Nano-Objects 17 (2019) 21-33, https://doi.org/10.1016/j.nanoso.2018.10.002.

[45] Joana Monteiro Baptista, Jagdeep S. Sagu, Upul Wijayantha KG, Killian Lobato, State-of-the-art materials for high power and high energy supercapacitors: Performance metrics and obstacles for the transition from lab to industrial scale – A critical approach, Chem. Eng. J. 374 (2019) 1153–1179, https://doi.org/10.1016/j.cej.2019.05.207.

[46] A. J. Bard, L. R. Faulkner, Electrochemical Methods: Fundamentals and Applications, 2nd Ed., John Wiley, New York, N.Y. USA, 2000.

[47] G. Saeed, S. Kumar, P. Bandyopadhyay, N.H. Kim, J.H. Lee, Hierarchical design of Cu-Ni$(OH)_2$/Cu-Mn_xO_y core/shell nanosheet arrays for ultra-high performance of asymmetric supercapacitor, Chem. Eng. J. 369 (2019) 705–715, https://doi.org/10.1016/j.cej.2019.03.124.

[48] T.C. Liu, W.G. Pell, B.E. Conway, Behavior of molybdem nitrides as materials for elecrochemcial capacitors, J. Electrochem. Soc. 145 (6) (1998) 1882–1888, https://doi.org/10.1149/1.1838571.

[49] Simon Fleischmann, James B. Mitchell, Ruocun Wang, Cheng Zhan, De-en Jiang, Volker Presser, Veronica Augustyn, Pseudocapacitance: From fundamental understanding to high power energy storage Materials, Chem. Rev. 120 (14) (2020) 6738–6782, https://doi.org/10.1021/acs.chemrev.0c00170.

[50] J.H. Albering, Structural chemistry of manganese dioxide and related compounds, Handbook of Battery Materials, 2nd Ed., 2011 Wiley-VCH Verlag GmbH & Co. KGaA.

[51] A.R. Selvaraj, H.J. Kim, K. Senthil, K. Prabakar, Cation intercalated one-dimensional manganese hydroxide nanorods and hierarchical mesoporous activated carbon nanosheets with ultrahigh capacitance retention asymmetric supercapacitors, J. Colloid Interf. Sci. 566 (2020) 485–494, https://doi.org/10.1016/j.jcis.2020.01.117.

[52] R.A. Aziz, R. Jose, Charge storage capability of tunnel MnO_2 and alkaline layered Na-MnO_2 as anode material for aqueous asymmetry supercapacitor, J. Electroanal. Chem. 799 (2017) 538–546, https://doi.org/10.1016/j.jelechem.2017.06.014.

[53] Zhi Yi Leong, Hui Ying Yang, A study of MnO_2 with different crystalline forms for pseudocapacitive desalination, ACS Appl. Mater. Interfaces 11 (14) (2019) 13176–13184, https://doi.org/10.1021/acsami.8b2088010.1021/acsami.8b20880.s001.

[54] Jianbo Zhu, Youlong Xu, Jie Wang, Jun Lin, Xiaofei Sun, Shengchun Mao, The effect of various electrolyte cations on electrochemical performance of polypyrrole/RGO based supercapacitors, Phys. Chem. Chem. Phys. 17 (43) (2015) 28666–28673, https://doi.org/10.1039/C5CP04080A.

[55] Bhupender Pal, Shengyuan Yang, Subramaniam Ramesh, Venkataraman Thangadurai, Rajan Jose, Electrolyte selection for supercapacitive devices: a critical review, Nanoscale Adv. 1 (10) (2019) 3807–3835, https://doi.org/10.1039/C9NA00374F.

[56] C.L. Yeh, H.C. Hsi, K.C. Li, C.H. Hou, Improved performance in capacitive deionization of activated carbonelectrodes with a tunable mesopore and micropore ratio, Desalination 367 (2015) 60–68, https://doi.org/10.1016/j.desal.2015.03.035.

[57] M. Kim, I. Oh, J. Kim, Hierarchical porous silicon carbide with controlled micropores and mesopores for electric double layer capacitors, J. Power Source. 282 (2015) 277–285, https://doi.org/10.1016/j.jpowsour.2015.02.040.

[58] K.H. Park, D.H. Kwak, Electrosorption and electrochemical properties of activated-carbon sheet electrode for capacitive deionization, J. Electroanal. Chem. 732 (2014) 66–73, https://doi.org/10.1016/j.jelechem.2014.08.020.

[59] D. W. Smith, Ionic hydration enthalpies, J. Chemical Education, 54(9) (1977) 540-542, https://pubs.acs.org/doi/10.1021/ed054p540.

[60] N. Pugazhenthiran, S.S. Gupta, A. Prabhath, M. Manikandan, J.R. Swathy, V. K. Raman, T. Pradeep, Cellulose derived graphenic fibers for capacitive desalination of brackish Water, ACS Appl. Mater. Interfaces 7 (36) (2015) 20156–20163, https://doi.org/10.1021/acsami.5b05510.

[61] H. Yoon, J. Lee, S. Kim, J. Yoon, Review of concepts and applications of electrochemical ion separation (EIONS) process, Sep. Purif. Technol. 215 (2019) 190–207, https://doi.org/10.1016/j.seppur.2018.12.071.

[62] S. Kaya, C. Kaya, A new equation based on ionization energies and electron affinities of atoms for calculating of group electronegativity, Comput. Theo. Chem. 1052 (2015) 42–46, https://doi.org/10.1016/j.comptc.2014.11.017.

[63] Andrew M. James, Croix J. Laconsay, John Morrison Galbraith, Charge-shift corrected electronegativities and the effect of bond polarity and substituents on covalent−ionic resonance energy, J. Phys. Chem. A 121 (27) (2017) 5190–5195, https://doi.org/10.1021/acs.jpca.7b02988.

[64] Z. Sun, L. Chai, M. Liu, Y. Shu, Q. Li, Y. Wang, D. Qiu, Effect of the electronegativity on the electrosorption selectivity of anions during capacitive deionization, Chemosphere 195 (2018) 282–290, https://doi.org/10.1016/j.chemosphere.2017.12.031.

[65] A. Subramani, J.G. Jacangelo, Treatment technologies for reverse osmosis concentrate volume minimization: A review, Sep. Purif. Technol. 122 (2014) 472–489, https://doi.org/10.1016/j.seppur.2013.12.004.

[66] Adewale S. Bello, Nabil Zouari, Dana A. Da'ana, John N. Hahladakis, Mohammad A. Al-Ghouti, An overview of brine management: Emerging desalination technologies, life cycle assessment, and metal recovery methodologies, J. Environ. Manag. 288 (2021) 112358, https://doi.org/10.1016/j.jenvman.2021.112358.

[67] Yolanda Belaustegui, Fabiola Pantò, Leire Urbina, Maria Angeles Corcuera, Arantxa Eceiza, Alessandra Palella, Claudia Triolo, Saveria Santangelo, Bacterial-cellulose-derived carbonaceous electrode materials for water desalination via capacitive method: The crucial role of defect sites, Desalination 492 (2020) 114596, https://doi.org/10.1016/j.desal.2020.114596.

[68] Dinh Viet Cuong, Po-Chang Wu, Nei-Ling Liu, Chia-Hung Hou, Hierarchical porous carbon derived from activated biochar as an eco-friendly electrode for the electrosorption of inorganic ions, Sep. Purif. Technol. 242 (2020) 116813, https://doi.org/10.1016/j.seppur.2020.116813.

[69] Alessandra P. Silva, Alexandre Argondizo, Patricia T. Juchen, Luís A.M. Ruotolo, Ultrafast capacitive deionization using rice husk activated carbon electrodes, Sep. Purif. Technol. 271 (2021) 118872, https://doi.org/10.1016/j.seppur.2021.118872.

[70] M.P. Maniscalco, C. Corrado, R. Volpe, A. Messineo, Evaluation of the optimal activation parameters for almond shell bio-char production for capacitive deionization, Biore. Technol. Rep. 11 (2020) 100435, https://doi.org/10.1016/j.biteb.2020.100435.

[71] Vengatesan Muthukumaraswamy Rangaraj, Anjali Achazhiyath Edathil, Yasun Y. Kannangara, Jang-Kun Song, Mohammad Abu Haija, Fawzi Banat, Tamarind shell derived N-doped carbon for capacitive deionization (CDI) studies, J. Electroanal. Chem. 848 (2019) 113307, https://doi.org/10.1016/j.jelechem.2019.113307.

[72] G. Bharath, K. Rambabu, F. Banat, A. Hai, A.F. Arangadi, N. Ponpandian, Enhanced electrochemical performances of peanut shell derived activated carbon and its Fe_3O_4 nanocomposites for capacitive deionization of Cr(VI) ions, Sci. Total Environ. 691 (2019) 713–726, https://doi.org/10.1016/j.scitotenv.2019.07.069.

[73] Joemer Adorna, Myra Borines, Van Dien Dang, Ruey-An Doong, Coconut shell derived activated biochar–manganese dioxide nanocomposites for high performance capacitive deionization, Desalination 492 492 (2020) 114602, https://doi.org/10.1016/j.desal.2020.114602.

[74] H.H. Kyaw, S.M. Al-Mashaikhi, M.T.Z. Myint, S. Al-Harthi, El-Said I. El-Shafey, M. Al-Abri, Activated carbon derived from the date palm leaflets as multifunctional electrodes in capacitive deionization system, Chem. Eng. Proc. Proc. Intensif. 161 (2021) 108311, https://doi.org/10.1016/j.cep.2021.108311.

[75] Minjun Kim, Hyunsoo Lim, Xingtao Xu, Md Shahriar A. Hossain, Jongbeom Na, Nur Nadia Awaludin, Jagrat Shah, Lok Kumar Shrestha, Katsuhiko Ariga, Ashok Kumar Nanjundan, Darren J. Martin, Joseph G. Shapter, Yusuke Yamauchi, Sorghum biomass-derived porous carbon electrodes for capacitive deionization and energy storage, Microp. Mesop. Mater. 312 (2021) 110757, https://doi.org/10.1016/j.micromeso.2020.110757.

[76] K. Rambabu, G. Bharath, Abdul Hai, Shaohong Luo, Kin Liao, Mohammad Abu Haija, Fawzi Banat, Mu. Naushad, Naushad, Development of watermelon rind derived activated carbon/manganese ferrite nanocomposite for cleaner desalination by capacitive deionization, J. Clean. Prod. 272 (2020) 122626, https://doi.org/10.1016/j.jclepro.2020.122626.

[77] J. Elisadiki, Y.A.C. Jande, R.L. Machunda, T.E. Kibona, Porous carbon derived from Artocarpus heterophyllus peels for capacitive deionization electrodes, Carbon 147 (2019) 582–593, https://doi.org/10.1016/j.carbon.2019.03.036.